Cell type-specific lipid storage changes in Parkinson's disease patient brains are recapitulated by experimental glycolipid disturbance

Oeystein Roed Brekk[a,1], Jonathan R. Honey[b,2], Seungil Lee[b], Penelope J. Hallett[a], and Ole Isacson[a,1]

[a]Neuroregeneration Institute, McLean Hospital/Departments of Neurology and Psychiatry, Harvard Medical School, Belmont, MA 02478 and [b]Neuroregeneration Institute, McLean Hospital/Harvard Medical School, Belmont, MA 02478

Edited by Solomon H. Snyder, Johns Hopkins University School of Medicine, Baltimore, MD, and approved September 2, 2020 (received for review February 17, 2020)

Neurons are dependent on proper trafficking of lipids to neighboring glia for lipid exchange and disposal of potentially lipotoxic metabolites, producing distinct lipid distribution profiles among various cell types of the central nervous system. Little is known of the cellular distribution of neutral lipids in the substantia nigra (SN) of Parkinson's disease (PD) patients and its relationship to inflammatory signaling. This study aimed to determine human PD SN neutral lipid content and distribution in dopaminergic neurons, astrocytes, and microglia relative to age-matched healthy subject controls. The results show that while total neutral lipid content was unchanged relative to age-matched controls, the levels of whole SN triglycerides were correlated with inflammation-attenuating glycoprotein non-metastatic melanoma protein B (GPNMB) signaling in human PD SN. Histological localization of neutral lipids using a fluorescent probe (BODIPY) revealed that dopaminergic neurons and midbrain microglia significantly accumulated intracellular lipids in PD SN, while adjacent astrocytes had a reduced lipid load overall. This pattern was recapitulated by experimental in vivo inhibition of glucocerebrosidase activity in mice. Agents or therapies that restore lipid homeostasis among neurons, astrocytes, and microglia could potentially correct PD pathogenesis and disease progression.

Parkinson's disease | glucocerebrosidase | lipids | neurons | astrocytes

Both neurons and glia depend on tight regulation and exchange of lipids for proper function. Typically through lipid transport mechanisms (1, 2), the continuous exchange of lipids is essential for maintaining physiological function as brain lipid content, transport, and distribution are complex and critical aspects of neuropathology. Recently, both clinical findings and experimental studies have implicated lipid storage and trafficking in the pathogenesis of Parkinson's disease (PD) and related disorders (3, 4). Reduced function of lysosomal hydrolases that are associated with lysosomal storage disorders increases the risk for PD and results in brain pathology similar to that seen in most sporadic and genetic forms of the disease (5–11).

One of the strongest genetic risk factors for PD is heterozygous loss-of-function mutations in *GBA1*, encoding the lysosomal hydrolase glucocerebrosidase (GCase) (12–14), a deficiency that causes systemic accumulation of its glycolipid substrate glucosylceramide (GlcCer). GCase activity is reduced with aging of both the human and murine brain (6, 15), and age is the overall greatest risk factor for developing PD (16). In contrast, the more severe loss of GCase activity in homozygous *GBA1* mutant carriers causes the lysosomal storage disease Gaucher disease (GD) (17). Conduritol beta epoxide (CBE), an irreversible inhibitor of GCase, causes widespread accumulation of GlcCer and related glycosphingolipids in mice. In this model, there is marked increase of high molecular weight alpha-synuclein (aSYN) and deposition of proteinase K-resistant aSYN resembling that seen in PD (18–20). aSYN is a constituent of the classical Lewy bodies and Lewy neurites (21) found in surviving dopaminergic neurons in postmortem PD materials as a standard pathological criterion for PD (22). aSYN has a lipid-binding domain, and aSYN protein–lipid interactions are potentially perturbed in PD (reviewed in refs. 17, 23, 24). We recently demonstrated that excessive aSYN can deposit into lipid compartments, and that this process is reversible under increased lysosomal β-hexosaminidase expression (25).

Several in vitro physiological studies have demonstrated that a reduction in neuronal neutral lipid storage or knockdown of fatty acid desaturases protects cultured neurons from degeneration (26–28). However, as neurons exhibit limited capacity to synthesize, metabolize, and transport lipid species under physiological conditions (29), other resident cells of the substantia nigra (SN), such as glial cells, are required to maintain lipid homeostasis in the brain. Astrocyte health and lipid exchange function—and microglial activation—are potentially central to PD pathogenesis and other age-dependent neurodegenerative diseases (30–33). Brain resident microglia can accumulate and generate lipids, which may propagate inflammatory processes through, for example, TREM2 binding of apolipoproteins

Significance

Recently, the field of Parkinson's disease biology has shifted attention away from pure proteinotoxic hypotheses to emphasize primary cellular insults, including glycolipid disturbances. In this work, dopaminergic neurons in the Parkinson's disease-vulnerable region of substantia nigra were found to accumulate neutral lipids, whereas in the same tissues, astrocytes have reduced lipid content, and resident microglia (a form of brain macrophage) show overall accumulation of lipids associated with inflammation. These changes were reproduced experimentally by blocking a specific lysosomal hydrolase in mice, generating a glycolipid accumulation in the animals. Based on these findings, it is reasonable to propose that restoring lipid homeostasis between neurons, astrocytes, and microglia could potentially influence PD pathogenesis and disease progression.

Author contributions: O.R.B., P.J.H., and O.I. designed research; O.R.B., J.R.H., and S.L. performed research; O.R.B., J.R.H., S.L., P.J.H., and O.I. analyzed data; and O.R.B., S.L., P.J.H., and O.I. wrote the paper.

The authors declare no competing interest.

This article is a PNAS Direct Submission.

[1]To whom correspondence may be addressed. Email: obrekk@mclean.harvard.edu or isacson@hms.harvard.edu.

[2]Present address: School of Clinical Medicine, Addenbrooke's Hospital/University of Cambridge, Cambridge, CB2 0QQ Cambridgeshire, UK.

This article contains supporting information online at https://www.pnas.org/lookup/suppl/doi:10.1073/pnas.2003021117/-/DCSupplemental.

First published October 15, 2020.

(34–38). Proinflammatory cytokines present in chronic conditions are attenuated by the binding of glycoprotein nonmetastatic melanoma protein B (GPNMB) to the CD44 receptor on astrocytes (39). In GD patient serum, GPNMB level is significantly correlated with disease severity (40), and GPNMB is increased in human PD SN and following CBE-induced glycolipid accumulation in mice (41).

There are surprisingly little data on lipid distribution patterns in PD-affected cell types given the relevance of lipid homeostasis, aSYN–lipid interactions, and lipidopathy-associated inflammatory signatures as they relate to PD (17, 41). In this study, we measured the differences in total lipid content and cellular distribution between PD and healthy subject (HS) SN and compared them with a lipid-associated neuroinflammatory signal, GPNMB. To quantify cell type-specific intracellular lipid content, colocalization analysis was performed on human postmortem SN sections that were costained for neutral lipids and markers of dopaminergic neurons, astrocytes, and microglia. Compared with HS SN, the lipid content of PD dopaminergic neurons and microglia was significantly higher, and that of astrocytes was significantly lower. To understand a possible mechanistic reason for this lipid distribution pattern, we used an in vivo mouse model of glycolipid dysregulation and attendant aSYN accumulation through GCase inhibition by CBE. This in vivo model recapitulated the lipid distribution pattern that we observed in human PD SN. Based on these data, we propose that PD is characterized by a unique neutral lipid distribution signature in neurons, astrocytes, and microglia that can be recapitulated experimentally by glycolipid dysregulation.

Results

Total Triglyceride Levels Correlate with GPNMB and Lipids Accumulate in Dopaminergic Neurons in Human PD SN. To investigate lipid perturbations that might accompany idiopathic PD pathology, postmortem dissected PD and HS SN (cohort information provided in *SI Appendix*, Table S2) were lipid-extracted and analyzed fluorometrically for changes in neutral lipid content. In whole-SN extracts, there were no significant changes in either triglycerides (TG) (Fig. 1*A*) or diglycerides (DG) (Fig. 1*B*) comparing PD SN and age-matched HS SN. However, TG abundance correlated significantly with GPNMB levels, a marker for lipid and inflammatory responses, in SN samples from the same subjects (Fig. 1*C*).

Given the correlation between lipid- and inflammation-associated GPNMB and total TG content (Fig. 1*C*) we searched for cell type-specific changes in neutral lipid distribution that might explain these findings. To this end, human postmortem PD and HS SN (cohort information provided in *SI Appendix*, Table S1) were labeled with the fluorescent neutral lipid probe BODIPY to visualize neutral lipid accumulation specifically within the neuropigmented dopaminergic neurons affected by the disease (Fig. 2*A*). In PD SN, neuropigmented cells appeared to have an overall increase in the $BODIPY^+$ signal relative to age-matched HS SN cells.

To obtain an unbiased quantification of the neutral lipid load in dopaminergic neurons, human SN sections were fluorescently colabeled for neutral lipids and tyrosine hydroxylase (TH) (Fig. 2*B*). For a highly sensitive measure of overlap between $BODIPY^+$ and TH^+ signals, these images were further analyzed using an automated deconvolution and segmentation workflow (42, 43). The analysis revealed a statistically significant, nearly twofold increase in lipid load within TH^+ dopaminergic neurons in PD SN (Fig. 2*C*). PD SN neurons had numerous lipid inclusions that colocalized with $aSYN^+$ inclusions (Fig. 2*D*). These inclusions were on average larger in the PD SN (Fig. 2*E*) and contained more neutral lipid relative to inclusion size (Fig. 2*F*). There was limited overlap of $BODIPY^+$ inclusions with the cell

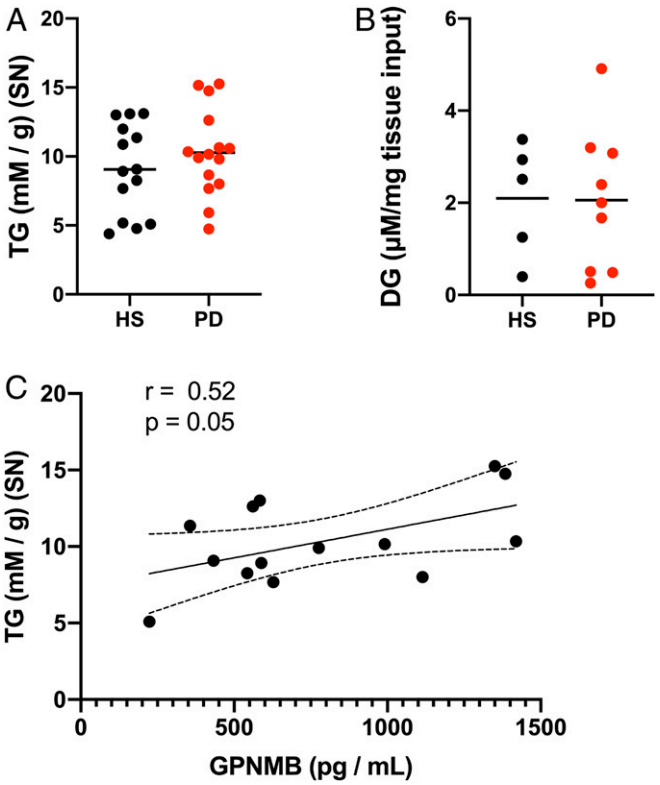

Fig. 1. Total TG levels correlate with GPNMB in human PD SN. (*A*) Fluorometric enzymatic measurements of TG (expressed as mM per g of tissue) from lipid-extracted postmortem human SN. (*B*) Fluorometric enzymatic measurements of DG (expressed as μM per mg of tissue) from samples treated as in *A*. (*C*) Cross-correlation plot of TG measurements from *A* against GPNMB measurements from the same subjects. The dashed lines in the correlation plot represent ± 95% confidence interval.

nucleus of neuromelanized neurons of the PD SN (*SI Appendix*, Fig. S1), indicating that majority of the lipid signal was cytosolic.

To assess whether the heterogenous $BODIPY^+$ signal within TH^+ dopaminergic neurons represents accumulated lipid droplets in PD SN, tissues were colabeled with a marker for perilipin-2, a ubiquitously expressed lipid droplet marker, which showed no overlap with $BODIPY^+$ fluorescence (*SI Appendix*, Fig. S2). The binding of lipids by perilipin-2 protein in lipid droplets is predicted to occur through noncovalent hydrogen bonds (44), which are of insufficient strength to stabilize lipids through the solvents used for standard paraffin-embedding procedures (45, 46). Therefore, the $BODIPY^+$ signal described in these paraffin-embedded postmortem human samples likely represents larger and more heterogenous lipid structures than perilipin-associated lipid droplets.

Astrocytes Have Reduced Neutral Lipid Content That Is Inversely Proportional to Lipid Content in Adjacent Dopaminergic Neurons in PD and Associated with $GFAP^+$ Immunoreactivity in PD SN. As GPNMB signaling is primarily associated with astrocytic and microglial responses to lipid induced stressors in humans and animal models, $BODIPY^+$ neutral lipids were visualized within adjacent $GFAP^+$ astrocytes in the same subject SN (Fig. 3*A*) to identify any changes in astrocytic lipid content or overall astrocyte abundance, as well as any relation to the dopaminergic neutral lipid phenotype. A sixfold increase in $GFAP^+$ immunoreactivity was observed in PD substantia nigra pars compacta (SNpc) relative to age-matched HS SNpc (Fig. 3*B* and *SI Appendix*, Fig. S3*A*), which coincided with a threefold reduction in

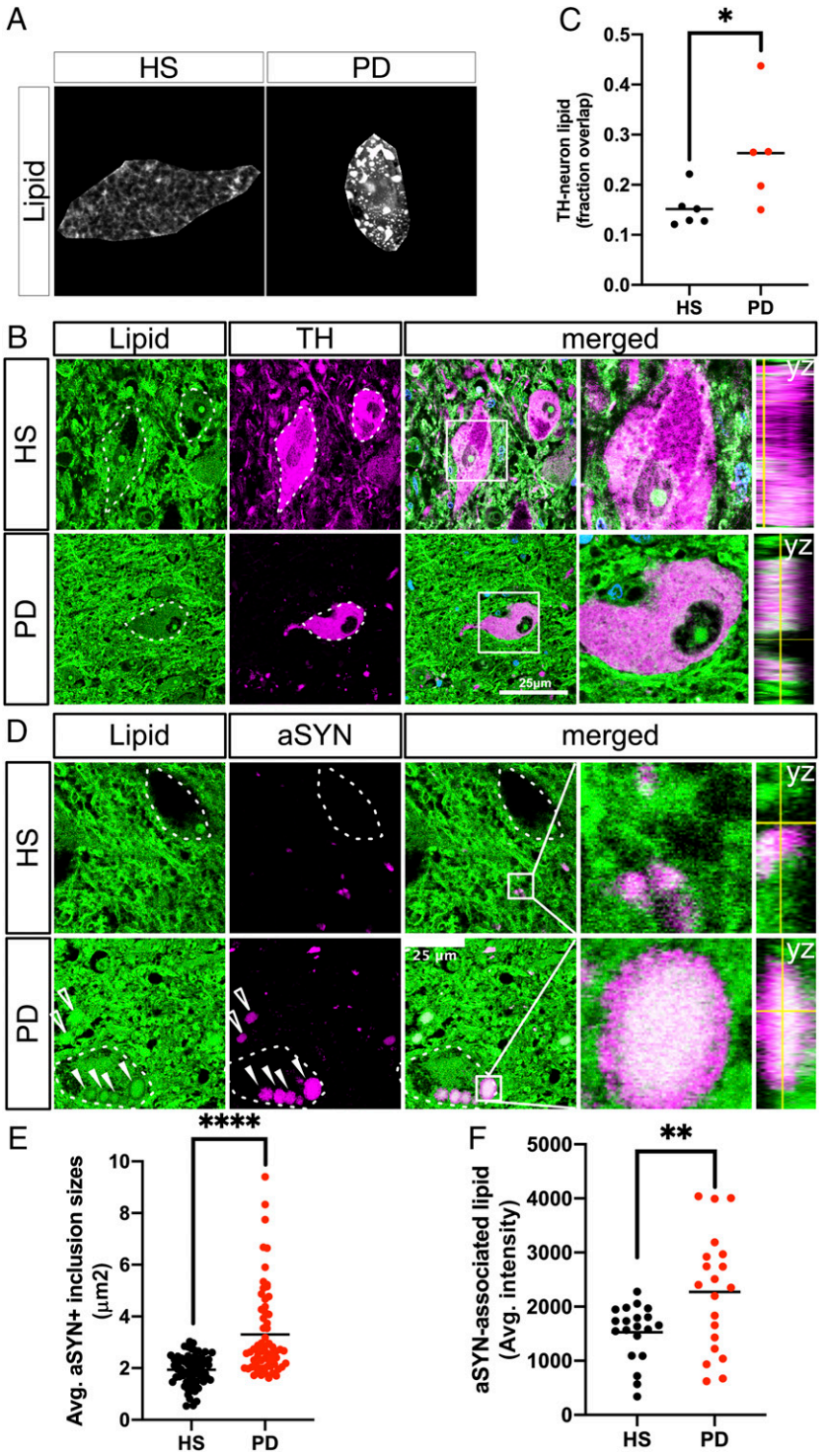

Fig. 2. Neutral lipids accumulate in PD patient brains relative to age-matched healthy subjects and localize to aSYN-rich inclusion bodies within dopaminergic neurons of the SN. (*A*) Fluorescent micrographs labeled for neutral lipids (BODIPY) (gray-scale) in neuromelanized dopaminergic neurons of the HS SN and PD SN. Neuropigmented cell profiles were manually isolated from the surroundings for clarity. (*B*) Representative micrographs of neutral lipids (BODIPY; green) and TH (magenta) colabeled neurons in HS SN and PD SN. Nuclei (TO-PRO; blue) are shown merged. The dotted line represents TH^+ cell outlines. Boxed insets are shown in higher magnification with orthogonal views on the right (scale bar: 25 µm). (*C*) Automated overlap coefficients of images colabeled as in *B* of the $BODIPY^+/TH^+$ area over the total $BODIPY^+$ area, expressed as lipid (fraction overlap). $^*P < 0.05$, $n = 5$ to 6 subject averages per group, $n = 3$ to 5 fields of view containing one or two cells per field (Z-stacks) per subject. The line indicates the mean, with individual values shown. (*D*) Representative micrograph of neutral lipid (green) and aSYN (magenta) in HS SN and PD SN. The dotted outline represents $neuromelanin^+$ cell profiles as identified by bright-field microscopy before confocal imaging. Boxed insets are shown in higher magnification with orthogonal views on the right. Filled arrowheads indicate intracellular Lewy bodies; empty arrowheads indicate Lewy body-like inclusions not associated with neuromelanized cell profiles (scale bar: 25 µm). (*E*) Quantification of the average size of $aSYN^+$ inclusions from five fields of view from HS SN and PD SN. $^{****}P < 0.0001$, $n = 60$ inclusions per group pooled from $n = 2$ subjects per group. (*F*) Quantification of the average intensity of the $BODIPY^+$ signal associated with each aSYN inclusion. The 20 largest aSYN inclusions per subject were selected for this analysis. $^{**}P < 0.01$, $n = 20$ per group pooled from $n = 2$ subjects per group.

astrocytic neutral lipid content (Fig. 3*C*). Cross-correlation analysis revealed a significant inverse relationship between astrocytic neutral lipid content and GFAP$^+$ immunoreactivity (Fig. 3*D*). In addition, astrocytic neutral lipid content was inversely correlated with neutral lipid storage in nearby dopaminergic neurons for each subject (Fig. 3*E*), showing that the reduced association of neutral lipids to astrocytes is coincident with both increased GFAP$^+$ immunoreactivity and increased neutral lipid association to adjacent dopaminergic neurons in the same patient samples.

SN Microglia Accumulate Neutral Lipids in PD. Next, to investigate the possibility of lipid changes in microglia accompanying the perturbed lipid distribution in neurons and astrocytes, HS and PD SN sections were costained with BODIPY and an antibody to TMEM119 (47) to visualize microglial neutral lipid storage and overall microglial abundance (Fig. 4*A*). PD SN contained more numerous and larger microglial cell profiles per field of view (Fig. 4*B* and *SI Appendix*, Fig. S3*B*), and PD SN microglia had more associated BODIPY$^+$ neutral lipids compared with age-matched HS SN microglia (Fig. 4*C*).

An Animal Model of Glycolipid Disturbance Recapitulates Neutral Lipid Distribution Patterns in PD Neurons and Glia. To explain the underlying mechanism for the observed PD cell type-specific neutral lipid distribution and correlation of GPNMB with TG in patients, we used a PD-relevant in vivo mouse model of glycolipid disturbance generated by GCase inhibition by CBE (*Materials and Methods*). This model replicates the proteinase K-resistant abnormal aSYN accumulation and aggregation, as well as the increased GPNMB levels, seen in human PD SN (18, 41). We measured the lipid localization in this mouse model

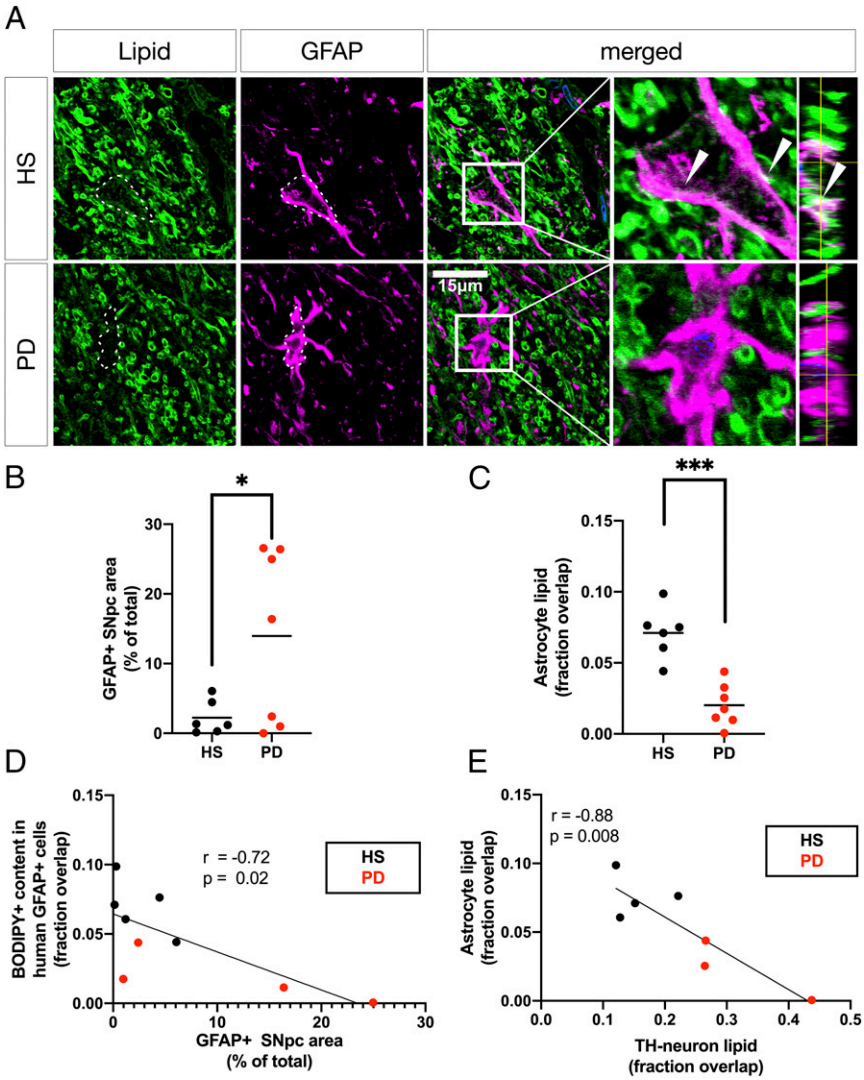

Fig. 3. Astrocytic neutral lipid storage is reduced in PD SN and correlated to neuronal neutral lipid content and overall astrocyte abundance. (*A*) Representative micrographs of BODIPY (green) and GFAP (magenta)-colabeled astrocytes in HS SNpc and PD SNpc. The dotted lines represent GFAP$^+$ outlines (scale bar: 15 µm). Nuclei (TO-PRO; blue) are shown in merged view. Boxed insets are shown in higher magnification with orthogonal views on the right. Arrowheads indicate GFAP$^+$-associated neutral lipid (BODIPY$^+$). (*B*) Quantification of SNpc GFAP$^+$ immunoreactivity in the indicated area of the SNpc as shown in *SI Appendix*, Fig. S3*A*, expressed as percentage of the total measured area occupied by the GFAP$^+$ signal. *$P < 0.05$, Welch's *t* test, $n = 6$ to 7 subject averages per group from whole-SNpc tile scans. (*C*) Automated overlap coefficients from images as in *A* of the BODIPY$^+$/GFAP$^+$ area over the total BODIPY$^+$ area, expressed as fraction overlapping. ***$P < 0.001$, each value averaged from $n = 3$ to 5 fields of view (Z-stacks) per subject. (*D*) Pearson's correlation comparing astrocytic lipid content measurements and GFAP$^+$ area measurements from *B*. (*E*) Cross-correlation plot of BODIPY$^+$/GFAP$^+$ coefficients from *C* and BODIPY$^+$/TH$^+$ coefficients from Fig. 2*C*.

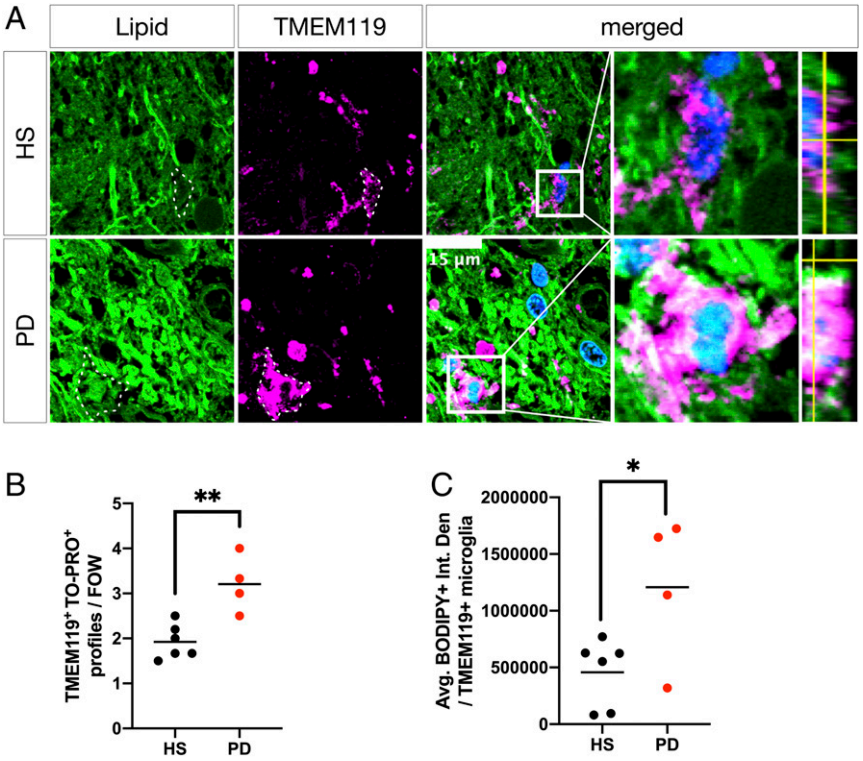

Fig. 4. Microglia accumulate neutral lipids in PD SN. (*A*) Representative micrographs of BODIPY (green) and TMEM119 (magenta) colabeled microglia in HS SN and PD SN. Boxed insets are shown in higher magnification with orthogonal views on the right. Dashed lines indicate TMEM119$^+$ microglial cell outlines. Nuclei (TO-PRO; blue) are shown in merged views (scale bar: 15 µm). (*B*) Average number of TMEM119$^+$/TO-PRO$^+$ microglia per randomly chosen field of view. $^{**}P < 0.01$, $n = 4$ to 6 subject averages per group, $n = 4$ to 6 fields of view per subject. (*C*) Quantification of BODIPY$^+$ neutral lipid (integrated density) associated with TMEM119$^+$/TO-PRO$^+$ microglial cell profiles. $^*P < 0.05$, $n = 4$ to 6 subject averages per group, $n = 5$ to 10 microglial cell profiles per subject.

using the same methodology as used in the patient samples, and found a significantly higher neutral lipid content in dopaminergic neurons (Fig. 5 *A* and *B*) and microglia (Fig. 5 *C* and *D*) and a lower neutral lipid content in astrocytes (Fig. 5 *E* and *F*) in the SN of CBE-treated mice compared to vehicle (VEH)-treated littermates, consistent with our observations in human PD SN. These findings in the mouse model of perturbed glycolipid homeostasis recapitulate the pattern of lipid distribution in dopaminergic neurons, astrocytes, and microglia seen in human PD.

Discussion

This investigation of postmortem human PD SN identified a correlation between whole-SN neutral lipid TG levels and anti-inflammatory GPNMB signaling. GPNMB is an anti-inflammatory signal shown to be a biomarker in the lysosomal storage disorder GD (39, 40), where it correlates with disease severity. Relevant to our study, GPNMB also has been shown to be up-regulated in idiopathic PD (41). Experimentally, GPNMB levels were increased by pharmacologic inhibition of GBA1, which causes a GD-like condition with subsequent alpha-synucleinopathy. However, a direct aSYN overexpression transgenic model did not cause GPNMB induction as seen in PD, indicating that the lipid disturbance is the key to the GPNMB induction. The total pool of lipids in the brain are derived from numerous sources, including in large part myelinated fiber bundles, all membrane cellular content, and individual cell types contained in the tissue.

Of critical importance to individual cell function and potentially to pathology is lipid homeostasis on a cell-to-cell basis. Therefore, we investigated neutral lipid content at cell type-specific levels. Through fluorescent labeling of neutral lipids, our experiments revealed specific differences in lipid content of neurons, astrocytes, and microglia in the SN of the human PD brain. These findings demonstrate that relative to age-matched HS SN controls, there is increased neutral lipid content in dopaminergic neurons and associated microglia, along with a concurrent reduction in adjacent astrocytes within the same subjects. Given that these cell type-specific changes occurred without a significant change in whole SN DG or TG abundance, this suggests an altered cell type-specific distribution of these lipids.

Interestingly, the accumulation of neutral lipids in dopaminergic neurons was linearly correlated with the loss of neutral lipids in astrocytes in the same subjects. Using a mouse model of a primary experimentally induced glycolipid challenge, we observed a similar pattern of lipid distribution as that seen in human PD. In these mice, SN dopaminergic neurons and adjacent microglia exhibited selective increases in neural lipid content, whereas astrocytes in the same tissue showed a reduction relative to VEH-treated controls.

What Pathophysiological Changes Would Create Such a Cell Type-Specific Lipid Pattern? Neurons have limited ability to oxidize fatty acids for energy (29), and proper trafficking of substrate to neighboring astrocytes is essential to avoid excessive lipid storage and generation of lipotoxic intermediates—particularly peroxidated lipid species—under conditions of high neuronal activity (48, 49). In *Drosophila* models of oxidative stress in neurons, there is an accumulation of lipids of net neutral charge in neighboring glia before neurodegeneration (50), which depends on interaction with apolipoprotein carriers (2). In response to neuronal oxidative stress, astrocytes up-regulate numerous genes associated with antioxidative detoxification and lipolytic processes to protect the surrounding cells (51). We cannot currently determine the precise cellular localization of

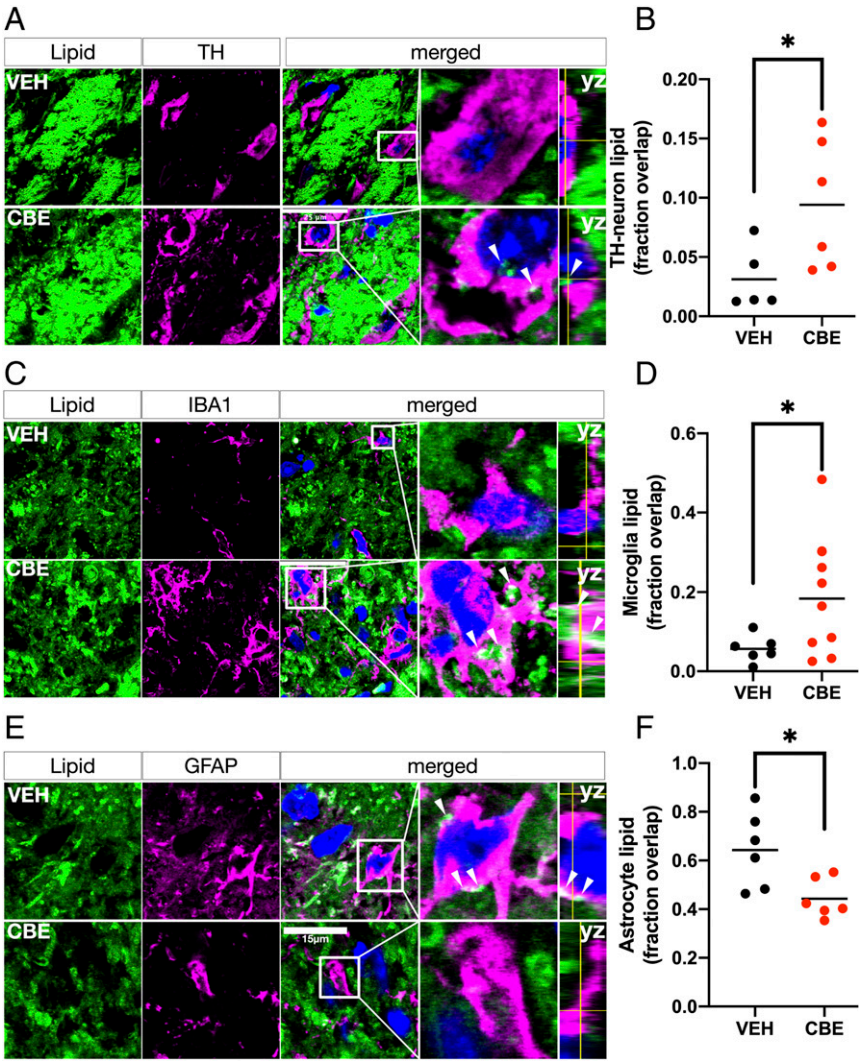

Fig. 5. The PD-associated multicellular neutral lipid compartmentalization phenotype can be recapitulated in an in vivo animal model of GCase inhibition based on charged sphingolipidosis. (*A*) Representative micrographs of BODIPY (green) and TH (magenta) colabeled neurons in the SN of mice treated systemically with the irreversible glucocerebrosidase inhibitor CBE or vehicle (VEH) for 28 d. Arrowheads indicate neuronal lipid deposits. Boxed insets are shown in higher magnification with orthogonal views on the right (scale bar: 25 μm). (*B*) Automated overlap coefficients from images as in *A* of the BODIPY$^+$/TH$^+$ area over the total BODIPY$^+$ area expressed as the fraction overlapping. *$P < 0.05$, $n = 5$ to 6 animals per group, 3 to 5 fields of view per animal). (*C*) Representative micrographs of BODIPY (green) and IBA1 (magenta) colabeled microglia in the SN of mice treated as in *A*. Outlines indicate astrocytic profiles. Arrowheads indicate astrocytic lipid deposits (scale bar: 25 μm). Boxed insets are shown in higher magnification with orthogonal views on the right. (*D*) Automated overlap coefficients from images as in *B* of the BODIPY$^+$/IBA1$^+$ area over the total BODIPY$^+$ area. **$P < 0.01$, $n = 6$ to 9 per group, $n = 3$ to 5 fields of view per animal. (*E*) Representative micrographs of BODIPY (green) and GFAP (magenta) colabeled astrocytes in the SN of mice treated as in *A*. Outlines indicate microglial profiles. Arrowheads indicate microglial lipid deposits (scale bar: 15 μm). Boxed insets are shown in higher magnification with orthogonal views on right. (*F*) Automated overlap coefficients from images as in *B* of the BODIPY$^+$/GFAP$^+$ area over the total BODIPY$^+$ area. *$P < 0.05$, $n = 6$ animals per group, $n = 3$ to 5 fields of view per animal. Nuclei (TO-PRO; blue) are shown in merged views for all images.

oxidized lipids in postmortem fixed human brain, even though the results presented here generally support the notion of a perturbed neuron-glia (astrocytes and/or microglia) shuttle as a central event in human PD. The significant inverse correlation found between neuronal and astrocytic lipid storage in the same subject samples emphasizes the potential importance of the neuron-glia lipid exchange pathway in PD.

The observed accumulation of neutral lipids within resident microglia of the PD SN could represent a cellular inflammatory state, as lipid deposition within cells of myeloid lineage is typically associated with activation of inflammatory signaling cascades (52, 53) and in response to increased lipid phagocytosis by microglia (36). In aging mice, lipid-rich microglia with elevated TNFα expression have been found in many brain regions (54). From our present results, it appears that PD SN has accelerated microglial lipid accumulation relative to age-matched HS SN. It is also noteworthy that in vivo systemic inhibition of GCase by chronic CBE insult recapitulated this pattern of cellular lipid content observed in human PD SN. Progressive decline of GCase activity is a feature of normal aging of both the human and murine brain (6, 15), and the decline is further accelerated in PD (6). Although little is known of direct crosstalk between lipid metabolic pathways in mammalian systems, insights from yeast models have revealed strong interdependence between neutral lipid and sphingolipid pathways. Specifically, impaired hydrolysis of TG perturbs sphingolipid synthesis through reduced substrate availability for the acylation reaction and lowered levels of phosphatidylinositol available for the initial inositol phosphate

linkage to ceramide species (55). As such, failure of synthetic and/or metabolic steps in one lipid pathway could perturb biochemically unrelated lipid species through altered substrate availability.

What Mechanisms or Cellular Interactions Generate the Pattern of Cellular Lipid Content Observed in PD SN? GCase activity in human PD SN is inversely correlated with the formation of high molecular weight insoluble aSYN (56), and *GBA1* overexpression in vivo rescues aSYN accumulation and dopaminergic neuron degeneration in aSYN overexpression-based models of the disease (57). Collectively, these data support the notion of lipid disturbance as a critical pathogenic event in PD (58–60). The lack of change in the total TG content comparing PD SN and age-matched controls possibly can be explained by the relative increases in microglial and neuronal lipids, with a corresponding loss in astrocytes that could mask an overall change. Nevertheless, the linear correlation between TG content and GPNMB signaling is interesting in the context of increased lipid content in microglia and neurons, as elevated GPNMB levels are known to act as a marker for similarly lipid-laden macrophages in GD patients and animal models (61). The demonstration that GCase inhibition in mice recapitulates the cellular lipid distribution changes seen in human PD SN indicates a potential mechanistic interplay between charged glycolipids and neutral lipids in both pathologies.

How do these results relate to the pathophysiological conditions involving cellular lipid content and transfer? An elevated lipid load in PD SN dopaminergic neurons is correlated with reduced SN astrocytic lipid content, and export of lipid-bound apolipoproteins through the ER secretory pathway is required for the initial clearing of lipids from the neuron cytosol, as inhibition of this step by brefeldin A treatment causes neuronal lipid accumulation (51, 62). The differences in lipid content of dopaminergic neurons and glia in the PD SN could be dependent on the endocytosis of neuron-released lipids by astrocytes involving lipoprotein receptor interactions, as saturation of astrocytic lipoprotein receptors by an excess of low-density lipoprotein can prevent neuron-astrocyte lipid transfer (51). Consequently, the differences in neutral lipid content observed in human PD astrocytes could be due to either increased astrocyte lipid export or decreased de novo neutral lipid synthesis. In microglia, lipids serve as sources of synthesis and storage of both eicosanoids and inflammatory cytokines and are functionally linked to both antigen presentation and clearance of pathogens (52, 63, 64). Outside the brain, lipid-laden "foam cell" macrophages have been described, and perturbed lipid homeostasis in these cells has been directly linked to the pathogenesis of atherosclerosis (65). In the aging brain, multiple cell types accumulate lipids, which coincide with elevated TNFα signaling (54), and lipid accumulation is correlated with a senescent cellular phenotype in the brain and elsewhere in the body (54, 66). In multiple sclerosis, lipid-laden macrophages found in the proximity of demyelinating active lesions have an eightfold elevation of GPNMB expression levels compared with inactive lesions (67). Microglia present in aging and Alzheimer's disease (AD) have elevated baseline levels of cytokines that are increased in response to proinflammatory stimuli, indicating that they are in a "primed" state (68). Single-cell RNA-seq datasets have identified unique, disease-associated subtypes of microglia in the AD brain with a proinflammatory phenotype and progressively upregulated apolipoprotein E (ApoE) expression (69). The link to ApoE levels is interesting, as in an in vivo animal model of demyelination, excessive myelin debris was taken up by resident microglia, causing accumulation and crystallization of microglial cholesterol in an ApoE-dependent fashion, which in turn increased inflammatory signaling (36). In this model, this change was reversed by stimulating cholesterol efflux from the affected cells. In cultured macrophages, inhibition of cholesterol efflux greatly increases GPNMB expression. Another interesting finding is the presence of lipid-accumulating microglia in both a $GRN^{-/-}$ transgenic mouse model of frontotemporal dementia and lipopolysaccharide (LPS)-treated wild-type mice in a model of chronic inflammation. The microglia in these models exhibit impaired phagocytosis, elevated reactive oxygen production, and increased cytokine secretion (35).

These original findings in PD patients and experimental animals of abnormal lipid accumulation in dopaminergic neurons and their surrounding microglia, with a corresponding reduction of lipid load in adjacent astrocytes, point to a primary role of lipid disturbances in the pathogenesis of this disease. Potentially, this cellular lipid distribution observed in the PD SN, also recapitulated in an animal model of abnormal lipid accumulation, also indicates a proinflammatory or chronic inflammatory condition based on the GPNMB data in our studies. Therapies and agents that reverse the pathological cell type-specific lipid distribution in the PD SN could serve to prevent and reduce the progression of PD and related neurodegenerative disorders.

Materials and Methods

Patients. Frozen postmortem and postfixed paraffin-embedded ventral midbrain tissues from male and female neurologically unaffected patients (HS) and age-matched sporadic PD patients were provided by the Harvard Brain Tissue Resource Center, part of the NIH NeuroBioBank. Cohort and diagnostic criteria are provided in *SI Appendix*, Tables S1 and S2. The average age of the HS cohort was 75.6 y (n = 6 for histology; n = 17 for biochemical analysis), and that of the for the PD cohort was 77.4 y (n = 9 for histology; n = 17 for biochemical analysis). Tissue was acquired with the full informed consent of patients or next of kin and was approved by Partners Human Research Committee and Institutional Review Board. All methods were performed in accordance with the relevant guidelines and regulations.

Mice. All animal procedures were performed in accordance with NIH guidelines and were approved by the Institutional Animal Care and Use Committee at McLean Hospital, Harvard Medical School. Animals were housed under standard conditions, in a 12-h dark/light cycle with ad libitum access to food and water. Male (n = 8) and female (n = 8) C57BL6/J mice at 1.5 mo of age (The Jackson Laboratory; RRID:IMSR_JAX:000664) were used.

In Vivo Pharmacologic Inhibition of GCase Activity. CBE (CAS 6090-95-5), a selective irreversible inhibitor of lysosomal GCase, was purchased from Millipore Sigma (catalog no. 234599). Mice received daily i.p. injections with CBE or DMSO vehicle (n = 9 per group) at 100 mg/kg for 21 to 28 d. Mice were killed at 24 h after the final i.p. injection.

Human Brain Biochemical Analysis. Neutral lipid species DG and TG were measured in total human SN lipid extracts (Lipid Extraction Kit ab211044; Abcam) using a colorimetric enzymatic assay (DG: Cell Biolabs, MET-5028; TG: Abcam, ab65336) according to the manufacturer's instructions. Measurements were normalized to total brain wet weight input from the lipid extraction step. Sample-matched GPNMB ELISA measurements from Moloney et al. (41), who used the same patient postmortem samples as in the present study, were used for the cross-correlation analysis with the TG measurements presented in Fig. 1. In brief, GPNMB ELISA measurements were done in human SN homogenates (25 μg of protein per sample) on an anti-GPNMB antibody-coated sandwich ELISA plate according to the manufacturer's instructions (Human Osteoactivin ELISA kit; RayBioTech, catalog no. ELH-Osteoactivin-1).

Immunohistochemistry. Postfixed, paraffin-embedded human brain specimens were sectioned at 8 μm through the coronal plane at the Beth Israel Deaconess Histology Core. Before histological analysis, the human tissue specimens were deparaffinized in xylene (2 × 5 min) and rehydrated in 100% and 95% ethanol gradients (3 min each). The xylene treatment removed the majority of lipids; however, lipids covalently bound to other substances, including lipoproteins and phospholipids, resist extraction by xylene used in routine histochemical processing (45, 46, 70), and specifically for the xylene incubation performed in the studies described herein.

Mice were perfused intracardially through the ascending aorta with physiological saline under pentobarbital anesthesia, followed by ice-cold 4%

paraformaldehyde. The brains were postfixed overnight in the same preparation of paraformaldehyde and subsequently transferred to 20% sucrose until sectioning. The brains were sectioned through the coronal plane in 40-μm increments, and each section throughout the striatum, hippocampus, and the ventral midbrain was collected. Immunohistochemical staining was performed in free-floating mouse tissues and on mounted human tissues. Primary antibodies included rabbit anti-TH (Pel-Freez, catalog no. P4010-1) (RRID:AB_461064), mouse anti-aSYN (Thermo Fisher Scientific, catalog no. AHB0261) (RRID:AB_2536241), rabbit anti-perilipin-2/ADFP (Novus, catalog no. NB110-40877) (RRID:AB_787904), mouse anti-GFAP (Agilent, catalog no. M0761) (RRID:AB_2109952), rabbit anti-GFAP (Agilent, catalog no. Z0334) (RRID:AB_10013382), rabbit anti-TMEM119 (Abcam, catalog no. ab185333, RRID:AB_2687894), and rabbit anti-IBA1 (Wako Chemicals, catalog no. 019–19741) (RRID:AB_839504). Nuclei were labeled with 1 μm of TO-PRO-3 iodide (Thermo Fisher Scientific, catalog no. T3605) for 15 min at room temperature. Secondary antibodies included goat anti-rabbit 647 (Thermo Fisher Scientific, catalog no. A27040) (RRID:AB_2536101) and goat anti-mouse 647 (Thermo Fisher Scientific, catalog no. A32728) (RRID:AB_2633277). Sections were washed three times in 1×PBS (Gibco, catalog no. 14190-144) and then blocked using 10% normal goat serum (Vector Laboratories, catalog no. S-1000) (RRID:AB_2336615) in PBS and 0.1% Triton X-100 for 1 h at room temperature. Primary antibodies were applied overnight at room temperature and subsequently for 48 h at 4° C for human tissues. For mouse tissues, primary incubation was done overnight at 4° C. After the primary antibody staining, sections were washed three times in 1× PBS, and secondary antibodies were applied for 1 h at room temperature.

Neutral Lipid Staining. After the secondary antibody labeling, sections were washed three times in PBS and then incubated for 1 h in 20 μg/mL BODIPY 493/503 (4,4-difluoro-1,3,5,7,8-pentamethyl-4-bora-3a,4a-diaza-s-indacene) (Invitrogen, D3922) diluted in 1× PBS. Then tissues were washed again in 1× PBS and immediately mounted and coverslipped using Mowiol.

Fluorescent Neutral Lipid Content Analysis. Mounted sections were optically sectioned with a Leica SM410 laser scanning confocal microscope with a Z-interval of 0.33 μm and a 100× objective set to 250% digital zoom. The BODIPY signal was autoexposed by the software (ZEN 2009), and all other cell markers had fixed exposure and cutoff values. Equal numbers of images from subjects in each comparison group (HS vs. PD and VEH vs. CBE) were acquired in each microscopy session to correct for any day-to-day variances in laser emission or other confounding variables. Each full Z-stack through a cellular plane consisted of 15 to 30 images, and between three and five fields of view per subject were chosen at random (based on the presence of neuromenlanized cell profiles identified using bright field microscopy, in the case of human subjects).

Whole stacks were analyzed using the Squassh plug-in (42) running in ImageJ. First, background was subtracted using a roll-ball algorithm with a 100-pixel window width. Each channel was segmented into structures with regularization set at 0.075 and minimum object intensity set at 0.150, using automated local intensity estimation and a Poisson-based noise model. The SD was estimated to 0.85 pixels in x and y and to 0.79 pixels in z based on the point spread function of our 100× objective. The colocalization measure C_{size} represents the fraction of the total volume above threshold in channel 1 (BODIPY) shared with volume above threshold in channel 2 (cell markers), divided by the full channel 1 volume above threshold in the whole image:

$$\frac{\sum(BODIPY\ \ object\ \ volume\ +\ cell\ \ marker\ \ object\ \ volume)}{\sum(BODIPY\ \ objects\ \ volume)}.$$

This coefficient is expressed as "lipid (fraction overlap)" on all y-axes. The experimenter was blinded to the patient group being imaged and analyzed.

Quantification of Astrocyte and Microglia Abundance and Microglial Neutral Lipid Content. GFAP-immunolabeled HS SN and PD SN whole-ventral midbrain sections were tile-scanned with a Keyence BZ-X700 fluorescent microscope using a 20× objective with fixed exposure and cutoff values. Stitched images containing the entirety of the tissue were thresholded in ImageJ (moments algorithm), and the indicated region of the SNpc was outlined manually. The "analyze particles" plug-in was used to quantify the percentage of SNpc occupied by the $GFAP^+$ signal above threshold relative to the measured area. $TMEM119^+$ microglia and $TO\text{-}PRO^+$ nuclei were imaged by confocal fluorescent microscopy in four to six randomly chosen fields of view within the SNpc, at 100× magnification. $TMEM119^+/TO\text{-}PRO^+$ microglia were manually counted, and the mean average cells per field of view per patient were reported. $TMEM119^+$ microglial neutral lipid content was determined by imaging of TMEM119 and BODIPY at fixed settings, manual isolation of $TMEM119^+/TO\text{-}PRO^+$ cell profiles, and measurements of the average integrated density of $BODIPY^+$ signal per cell. The experimenter was blinded to the patient group being imaged and analyzed.

Quantification of aSYN-Associated $BODIPY^+$ Neutral Lipid Signal. For these analyses, the $BODIPY^+$ $aSYN^+$ signal was imaged by confocal microscopy using fixed values for exposure and cutoff. The $aSYN^+$ signal was thresholded in ImageJ (moments algorithm, size cutoff at 0.30 and circularity set at 0.1 to 1.0) and used to mask the $BODIPY^+$ channel. The thresholded aSYN channel was measured using the "analyze particles" function, and the average size of each inclusion per field of view was plotted. The masked $BODIPY^+$ channel was z-projected (sum slices), and the integrated density of the $BODIPY^+$ signal was measured from the 10 largest inclusions/field of view. The experimenter was blinded to group conditions during imaging and analysis.

Statistics. GraphPad Prism 8.0 was used for all statistical analyses. Two-tailed parametric t tests were used for single comparisons. In the event of significantly different variances, Welch's correction was used. For correlation analysis, Pearson's r was computed. P values are indicated in the figure legends. All graphs include mean values with individual data points shown. Post hoc power analysis confirmed our group sizes as sufficient to reliably detect differences >35% with 80% power (at $P < 0.05$). Outlier analysis was done using the ROUT algorithm with a Q value of 2%.

Data Availability Statement. All data supporting the findings of this study are provided in the main text and *SI Appendix*.

ACKNOWLEDGMENTS. This research was supported by the NIH/National Institute of Neurological Disorders and Stroke (R01 NS092667, to P.J.H.), NIH/National Institute on Aging (R01 AG060195, to O.I.), the US Department of Defense (W81XWH2010368, to O.I.; W81XWH2010371, to P.J.H.), the Consolidated Anti-Aging Foundation (O.I.), the Orchard Foundation (O.I.), and the Harold and Ronna Cooper Postdoctoral Fellowship for Parkinson's Disease Research (O.R.B.).

1. R. W. Mahley, Central nervous system lipoproteins: ApoE and regulation of cholesterol metabolism. *Arterioscler. Thromb. Vasc. Biol.* **36**, 1305–1315 (2016).
2. L. Liu, K. R. MacKenzie, N. Putluri, M. Maletić-Savatić, H. J. Bellen, The glia-neuron lactate shuttle and elevated ROS promote lipid synthesis in neurons and lipid droplet accumulation in glia via APOE/D. *Cell Metab.* **26**, 719–737.e6 (2017).
3. C. J. H. M. Klemann *et al.*, Integrated molecular landscape of Parkinson's disease. *NPJ Parkinsons Dis.* **3**, 14 (2017).
4. K. J. Billingsley, S. Bandres-Ciga, S. Saez-Atienzar, A. B. Singleton, Genetic risk factors in Parkinson's disease. *Cell Tissue Res.* **373**, 9–20 (2018).
5. C. B. Do *et al.*, Web-based genome-wide association study identifies two novel loci and a substantial genetic component for Parkinson's disease. *PLoS Genet.* **7**, e1002141 (2011).
6. E. M. Rocha *et al.*, Progressive decline of glucocerebrosidase in aging and Parkinson's disease. *Ann. Clin. Transl. Neurol.* **2**, 433–438 (2015).
7. G. Wu *et al.*, Decreased activities of lysosomal acid alpha-D-galactosidase A in the leukocytes of sporadic Parkinson's disease. *J. Neurol. Sci.* **271**, 168–173 (2008).
8. R. Inzelberg, A. D. Korczyn, Parkinsonism in adult-onset GM2 gangliosidosis. *Mov. Disord.* **9**, 375–377 (1994).
9. Y. Saito, K. Suzuki, C. M. Hulette, S. Murayama, Aberrant phosphorylation of alpha-synuclein in human Niemann-Pick type C1 disease. *J. Neuropathol. Exp. Neurol.* **63**, 323–328 (2004).
10. B. R. Smith *et al.*, Neuronal inclusions of α-synuclein contribute to the pathogenesis of Krabbe disease. *J. Pathol.* **232**, 509–521 (2014).
11. E. Roze *et al.*, Dystonia and parkinsonism in GM1 type 3 gangliosidosis. *Mov. Disord.* **20**, 1366–1369 (2005).
12. N. Tayebi *et al.*, Gaucher disease with parkinsonian manifestations: Does glucocerebrosidase deficiency contribute to a vulnerability to parkinsonism? *Mol. Genet. Metab.* **79**, 104–109 (2003).
13. M. A. Nalls *et al.*, A multicenter study of glucocerebrosidase mutations in dementia with Lewy bodies. *JAMA Neurol.* **70**, 727–735 (2013).
14. E. Sidransky *et al.*, Multicenter analysis of glucocerebrosidase mutations in Parkinson's disease. *N. Engl. J. Med.* **361**, 1651–1661 (2009).
15. P. J. Hallett *et al.*, Glycosphingolipid levels and glucocerebrosidase activity are altered in normal aging of mouse brain. *Neurobiol. Aging* **67**, 189–200 (2018).
16. T. J. Collier, N. M. Kanaan, J. H. Kordower, Ageing as a primary risk factor for Parkinson's disease: Evidence from studies of non-human primates. *Nat. Rev. Neurosci.* **12**, 359–366 (2011).

17. P. J. Hallett, S. Engelender, O. Isacson, Lipid and immune abnormalities causing age-dependent neurodegeneration and Parkinson's disease. *J. Neuroinflammation* **16**, 153 (2019).
18. E. M. Rocha *et al*., Sustained systemic glucocerebrosidase inhibition induces brain α-synuclein aggregation, microglia and complement C1q activation in mice. *Antioxid. Redox Signal.* **23**, 550–564 (2015).
19. Y. H. Xu *et al*., Accumulation and distribution of α-synuclein and ubiquitin in the CNS of Gaucher disease mouse models. *Mol. Genet. Metab.* **102**, 436–447 (2011).
20. S. P. Sardi *et al*., CNS expression of glucocerebrosidase corrects α-synuclein pathology and memory in a mouse model of Gaucher-related synucleinopathy. *Proc. Natl. Acad. Sci. U.S.A.* **108**, 12101–12106 (2011).
21. M. G. Spillantini *et al*., α-synuclein in Lewy bodies. *Nature* **388**, 839–840 (1997).
22. W. Poewe *et al*., Parkinson disease. *Nat. Rev. Dis. Primers* **3**, 17013 (2017).
23. O. Isacson, O. R. Brekk, P. J. Hallett, Novel results and concepts emerging from lipid cell biology relevant to degenerative brain aging and disease. *Front. Neurol.* **10**, 1053 (2019).
24. S. Fanning, D. Selkoe, U. Dettmer, Parkinson's disease: Proteinopathy or lipidopathy? *NPJ Parkinsons Dis.* **6**, 3 (2020).
25. O. R. Brekk *et al*., Upregulating β-hexosaminidase activity in rodents prevents α-synuclein lipid associations and protects dopaminergic neurons from α-synuclein-mediated neurotoxicity. *Acta Neuropathol. Commun.* **8**, 127 (2020).
26. S. Fanning *et al*., Lipidomic analysis of α-synuclein neurotoxicity identifies stearoyl CoA desaturase as a target for Parkinson treatment. *Mol. Cell* **73**, 1001–1014.e8 (2019).
27. T. Imberdis *et al*., Cell models of lipid-rich α-synuclein aggregation validate known modifiers of α-synuclein biology and identify stearoyl-CoA desaturase. *Proc. Natl. Acad. Sci. U.S.A.* **116**, 20760–20769 (2019).
28. B. M. Vincent *et al*., Inhibiting stearoyl-CoA desaturase ameliorates α-synuclein cytotoxicity. *Cell Rep.* **25**, 2742–2754.e31 (2018).
29. P. Schönfeld, G. Reiser, Why does brain metabolism not favor burning of fatty acids to provide energy? Reflections on disadvantages of the use of free fatty acids as fuel for brain. *J. Cereb. Blood Flow Metab.* **33**, 1493–1499 (2013).
30. C. Yin *et al*., ApoE attenuates unresolvable inflammation by complex formation with activated C1q. *Nat. Med.* **25**, 496–506 (2019).
31. J. F. Arboleda-Velasquez *et al*., Resistance to autosomal dominant Alzheimer's disease in an APOE3 Christchurch homozygote: A case report. *Nat. Med.* **25**, 1680–1683 (2019).
32. J. I. Vélez *et al*., APOE*E2 allele delays age of onset in PSEN1 E280A Alzheimer's disease. *Mol. Psychiatry* **21**, 916–924 (2016).
33. F. L. Yeh, Y. Wang, I. Tom, L. C. Gonzalez, M. Sheng, TREM2 binds to apolipoproteins, including APOE and CLU/APOJ, and thereby facilitates uptake of amyloid-beta by microglia. *Neuron* **91**, 328–340 (2016).
34. A. Khatchadourian, S. D. Bourque, V. R. Richard, V. I. Titorenko, D. Maysinger, Dynamics and regulation of lipid droplet formation in lipopolysaccharide (LPS)-stimulated microglia. *Biochim. Biophys. Acta* **1821**, 607–617 (2012).
35. J. Marschallinger *et al*., Lipid-droplet-accumulating microglia represent a dysfunctional and proinflammatory state in the aging brain. *Nat. Neurosci.* **23**, 194–208 (2020).
36. L. Cantuti-Castelvetri *et al*., Defective cholesterol clearance limits remyelination in the aged central nervous system. *Science* **359**, 684–688 (2018).
37. P. L. Poliani *et al*., TREM2 sustains microglial expansion during aging and response to demyelination. *J. Clin. Invest.* **125**, 2161–2170 (2015).
38. J. D. Ulrich, T. K. Ulland, M. Colonna, D. M. Holtzman, Elucidating the role of TREM2 in Alzheimer's disease. *Neuron* **94**, 237–248 (2017).
39. M. L. Neal, A. M. Boyle, K. M. Budge, F. F. Safadi, J. R. Richardson, The glycoprotein GPNMB attenuates astrocyte inflammatory responses through the CD44 receptor. *J. Neuroinflammation* **15**, 73 (2018).
40. V. Murugesan *et al*., Validating glycoprotein non-metastatic melanoma B (gpNMB, osteoactivin), a new biomarker of Gaucher disease. *Blood Cells Mol. Dis.* **68**, 47–53 (2018).
41. E. B. Moloney, A. Moskites, E. J. Ferrari, O. Isacson, P. J. Hallett, The glycoprotein GPNMB is selectively elevated in the substantia nigra of Parkinson's disease patients and increases after lysosomal stress. *Neurobiol. Dis.* **120**, 1–11 (2018).
42. A. Rizk *et al*., Segmentation and quantification of subcellular structures in fluorescence microscopy images using Squassh. *Nat. Protoc.* **9**, 586–596 (2014).
43. G. Paul, J. Cardinale, I. F. Sbalzarini, Coupling image restoration and segmentation: A generalized linear model/bregman perspective. *Int. J. Comput. Vis.* **104**, 69–93 (2013).
44. C. P. Najt *et al*., Structural and functional assessment of perilipin 2 lipid binding domain(s). *Biochemistry* **53**, 7051–7066 (2014).
45. M. C. Berenbaum, Staining of bound lipids. *Nature* **174**, 190 (1954).
46. M. C. Berenbaum, The histochemistry of bound lipids. *J. Cell Sci.* **s3-99**, 231–242 (1958).
47. M. L. Bennett *et al*., New tools for studying microglia in the mouse and human CNS. *Proc. Natl. Acad. Sci. U.S.A.* **113**, E1738–E1746 (2016).
48. M. A. Aon, N. Bhatt, S. C. Cortassa, Mitochondrial and cellular mechanisms for managing lipid excess. *Front. Physiol.* **5**, 282 (2014).
49. I. J. Reynolds, T. G. Hastings, Glutamate induces the production of reactive oxygen species in cultured forebrain neurons following NMDA receptor activation. *J. Neurosci.* **15**, 3318–3327 (1995).
50. L. Liu *et al*., Glial lipid droplets and ROS induced by mitochondrial defects promote neurodegeneration. *Cell* **160**, 177–190 (2015).
51. M. S. Ioannou *et al*., Neuron-astrocyte metabolic coupling protects against activity-induced fatty acid toxicity. *Cell* **177**, 1522–1535 (2019).
52. M. H. den Brok, T. K. Raaijmakers, E. Collado-Camps, G. J. Adema, Lipid droplets as immune modulators in myeloid cells. *Trends Immunol.* **39**, 380–392 (2018).
53. P. T. Bozza, J. P. B. Viola, Lipid droplets in inflammation and cancer. *Prostaglandins Leukot. Essent. Fatty Acids* **82**, 243–250 (2010).
54. M. K. Shimabukuro *et al*., Lipid-laden cells differentially distributed in the aging brain are functionally active and correspond to distinct phenotypes. *Sci. Rep.* **6**, 23795 (2016).
55. S. Rajakumari, R. Rajasekharan, G. Daum, Triacylglycerol lipolysis is linked to sphingolipid and phospholipid metabolism of the yeast Saccharomyces cerevisiae. *Biochim. Biophys. Acta* **1801**, 1314–1322 (2010).
56. O. R. Brekk, A. Moskites, O. Isacson, P. J. Hallett, Lipid-dependent deposition of alpha-synuclein and Tau on neuronal Secretogranin II-positive vesicular membranes with age. *Sci. Rep.* **8**, 15207 (2018).
57. E. M. Rocha *et al*., Glucocerebrosidase gene therapy prevents α-synucleinopathy of midbrain dopamine neurons. *Neurobiol. Dis.* **82**, 495–503 (2015).
58. W. P. Gai *et al*., In situ and in vitro study of colocalization and segregation of α-synuclein, ubiquitin, and lipids in Lewy bodies. *Exp. Neurol.* **166**, 324–333 (2000).
59. K. Araki *et al*., Synchrotron FTIR micro-spectroscopy for structural analysis of Lewy bodies in the brain of Parkinson's disease patients. *Sci. Rep.* **5**, 17625 (2015).
60. S. H. Shahmoradian *et al*., Lewy pathology in Parkinson's disease consists of crowded organelles and lipid membranes. *Nat. Neurosci.* **22**, 1099–1109 (2019).
61. G. Kramer *et al*., Elevation of glycoprotein nonmetastatic melanoma protein B in type 1 Gaucher disease patients and mouse models. *FEBS Open Bio* **6**, 902–913 (2016).
62. R. D. Klausner, J. G. Donaldson, J. Lippincott-Schwartz, A. Brefeldin, Brefeldin A: Insights into the control of membrane traffic and organelle structure. *J. Cell Biol.* **116**, 1071–1080 (1992).
63. R. C. N. Melo *et al*., Lipid bodies in inflammatory cells: Structure, function, and current imaging techniques. *J. Histochem. Cytochem.* **59**, 540–556 (2011).
64. R. V. Farese Jr., T. C. Walther, Lipid droplets finally get a little R-E-S-P-E-C-T. *Cell* **139**, 855–860 (2009).
65. Y. Yuan, P. Li, J. Ye, Lipid homeostasis and the formation of macrophage-derived foam cells in atherosclerosis. *Protein Cell* **3**, 173–181 (2012).
66. R. Galupa *et al*., Senescent intimal foam cells are deleterious at all stages of atherosclerosis. *Science* **354**, 472–477 (2016).
67. D. A. E. Hendrickx *et al*., Gene expression profiling of multiple sclerosis pathology identifies early patterns of demyelination surrounding chronic active lesions. *Front. Immunol.* **8**, 1810 (2017).
68. K. I. Mosher, T. Wyss-Coray, Microglial dysfunction in brain aging and Alzheimer's disease. *Biochem. Pharmacol.* **88**, 594–604 (2014).
69. H. Keren-Shaul *et al*., A unique microglia type associated with restricting development of Alzheimer's disease. *Cell* **169**, 1276–1290.e17 (2017).
70. V. Carriel, F. Campos, J. Aneiros-Fernández, J. Kiernan, "Tissue Fixation and Processing for the Histological Identification of Lipids" in *Histochemistry of Single Molecules: Methods and Protocols*, (Springer, New York, 2017), pp. 197–207.